RSC Applied Interfaces

ROYAL SOCIETY OF CHEMISTRY

PAPER

View Article Online
View Journal

Cite this: DOI: 10.1039/d6lf00119j

Efficient prediction of effective bandgap and optical absorption in InAs/InAsSb type-II superlattices using localization landscape theory

Zhi-Jie Wu, [a] Łukasz Kubiszyn,[b] Krystian Michalczewski,[b] Dariusz Smoczyński,[b] Piotr Martyniuk [c] and Yuh-Renn Wu *[ad]

Ga-free InAs/InAsSb type-II superlattices (T2SLs) are promising absorber materials for mid-wave and long-wave infrared (MWIR and LWIR) photodetectors, yet quantitative modeling of their optically active bandgaps and absorption remains challenging due to strain and quantum confinement effects. In this work, the localization landscape (LL) theory is applied to efficiently predict effective bandgaps and optical absorption in strained InAs/InAsSb superlattices without explicitly solving the Schrödinger eigenvalue problem. The LL framework is coupled with strain-induced deformation potential theory to obtain effective quantum confinement potentials, from which absorption coefficients are directly evaluated. The calculated absorption spectra are quantitatively compared with absorption coefficients extracted from experimentally measured responsivity of MWIR and LWIR photodetectors. Excellent agreement is obtained in absorption onset energies, with LL-predicted optically active bandgaps matching Schrödinger-based calculations within an RMSE of 5.395 meV, and experimental cutoff energies within 5.502 meV. These results demonstrate that the LL framework serves as a computationally efficient and physically consistent alternative to eigenstate-based solvers for modeling disordered superlattice absorbers relevant to infrared photodetector design.

Received 14th April 2026,
Accepted 26th May 2026

DOI: 10.1039/d6lf00119j

rsc.li/RSCApplInter

I. Introduction

Reducing size, cost, weight, and power consumption is a primary driver for modern infrared (IR) imaging development. This objective is best addressed through high operating temperature (HOT) photodetectors,[1–5] which eliminate the need for bulky cryogenic cooling. However, achieving reliable HOT operation requires not only high crystalline quality but also modeling approaches capable of capturing the complex quantum and disorder effects inherent to nanoscale heterostructures. Ga-free InAs/InAsSb type-II superlattices (T2SLs) have recently attracted significant attention as an alternative to HgCdTe and conventional InAs/GaSb systems due to their long minority carrier lifetimes and high tunability.[6–8] By suppressing Ga-related native defects that act as Shockley–Read–Hall (SRH) recombination centres,[9–12] these structures enable improved performance in the MWIR and LWIR spectral regimes.[13] In this work, we adopt the localization landscape (LL) theory coupled with the strain-induced deformation potentials as a unified and physically grounded framework to describe carrier confinement, effective bandgap, and optical absorption in strained InAs/InAsSb T2SLs. The LL approach provides effective quantum potentials for electrons and holes without explicitly solving for eigenstates, naturally incorporating disorder-induced localization and quantum confinement effects.[14–17] Within this framework, all effective bandgaps and absorption coefficients discussed in this study are extracted from the LL model. Selected Schrödinger-based eigenstate calculations are additionally employed for validation purposes, confirming the accuracy of the LL-based description while highlighting its substantial computational efficiency. Owing to its computational efficiency and physical transparency, the LL framework is well-suited for modeling optical absorption in InAs/InAsSb T2SLs while capturing essential quantum confinement and localization effects. In this study, the LL approach is employed to investigate the absorption characteristic of MWIR and LWIR InAs/InAsSb superlattice (SL) photodetectors and compare with experimental results in a wide spectrum range.

[a] Graduate Institute of Photonics and Optoelectronics and Department of Electrical Engineering, National Taiwan University, Taipei 10617, Taiwan.
E-mail: yrwu@ntu.edu.tw
[b] VIGO Photonics S.A., 129/133 Poznańska Str., 05-850 Ożarów Mazowiecki, Poland
[c] Institute of Applied Physics, Military University of Technology, 2 Kaliskiego St., 00-908 Warsaw, Poland
[d] Center for Quantum Science and Engineering, National Taiwan University, Taipei 10617, Taiwan

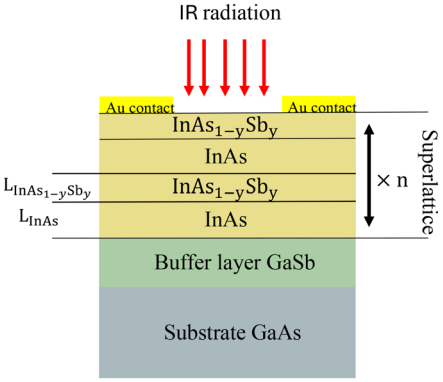

Fig. 1 Schematic illustration of the InAs/InAsSb T2SLs absorber structure investigated in this work. This thickness and composition are listed in Table 1.

II. Device structure and experimental methods

The studied cases include representative experimentally realized MWIR and LWIR SL absorbers with different layer thicknesses and antimony compositions, designed to capture the effects of strain, alloy disorder, and quantum confinement, as schematically illustrated in Fig. 1. These structures serve as realistic platforms for evaluating the applicability of the LL framework under practical device conditions. The key structural parameters of the MWIR and LWIR SL absorbers investigated in this work are summarized in Table 1. Here, d_{SL} denotes the total thickness of the superlattice absorber, λ_{cutoff} represents the cutoff wavelength defined as the wavelength at which the responsivity decreases to half of its maximum value, and d_{GaAs} denotes the thickness of the GaAs substrate.

The sample labels (L-z and M-z) indicate LWIR and MWIR designs, respectively, where the index z corresponds to the cutoff wavelength in micrometers rounded to one decimal place. For example, the sample labeled L-16.6 corresponds to a cutoff wavelength of 16.56 μm. The corresponding cutoff wavelengths are summarized in Table 1.

In InAs/InAsSb T2SLs, the effective bandgap and cutoff wavelength can be tuned by adjusting the SL period and the Sb composition through strain-balanced design. Such band engineering is well established and forms the basis for MWIR and LWIR device optimization.[18–20]

Based on these design considerations, the investigated structures were grown by molecular beam epitaxy (MBE) using a RIBER Compact-21DZ system on semi-insulating GaAs (001) substrates. GaAs substrates were selected due to their lower cost, larger wafer availability, and mature growth technology compared to GaSb substrates. Although GaSb (001) substrates offer better lattice matching for antimonide-based superlattices, a GaSb buffer layer combined with an interfacial misfit (IMF) array was employed to accommodate the lattice mismatch, which has been shown to effectively mitigate the effects of lattice mismatch.[21]

To manage the significant lattice mismatch of approximately 7.8% between the GaAs substrate and the SL layers, a GaSb buffer layer utilizing an interfacial misfit (IMF) dislocation array was initially deposited. This IMF buffer serves as a high-quality virtual substrate. The InAs/InAsSb SLs were designed to be strain-balanced to the GaSb buffer. The individual SL layer thicknesses and the composition within the InAsSb layers were precisely engineered to ensure that the overall net lattice constant of the SL remained strain-balanced and closely matched to the underlying GaSb buffer, maintaining high structural integrity throughout the heterostructure was confirmed by the High-Resolution X-ray Diffraction (HRXRD) measurements shown in Fig. 10 in the Appendix section. Following the epitaxial growth, device fabrication was carried out through a simple processing sequence involving photoresist masking and the electrolytic deposition of Au contacts to form lateral photoconductors. For experimental characterization, the fabricated devices were mounted on thermoelectric coolers, and their spectral responsivity was measured using a spectrophotometer.

IIII. Theoretical model and simulation framework

For this research, we employed an in-house one-dimensional drift-diffusion charge-control (1D-DDCC) solver to model the band structure and optical absorption of the strained InAs/InAsSb T2SL (Fig. 2). To analyze these properties, a simulation framework combining strain calculation, the Poisson and drift-diffusion equation, and

Table 1 Structural parameters and cutoff wavelengths of InAs/InAsSb T2SL samples, ordered by their cutoff wavelength within each spectral range. Here, $L_{contact}$ denotes the distance between the Au contacts

	L-16.6	L-14.4	L-10.7	L-8.7	M-7	M-6
L_{InAs} (nm)	10.86	8.14	7.87	9.93	3.67	3.48
$L_{InAs_{1-y}Sb_y}$ (nm)	3.41	2.58	2.47	3.97	1.30	1.26
$L_{contact}$ (nm)	2.43	2.36	1.97	1.72	2.77	3.09
y_{Sb}	0.42	0.44	0.38	0.30	0.35	0.335
λ_{cutoff} (μm)	16.56	14.44	10.66	8.71	6.98	5.98
T (K)	195	195	230	300	300	300
d_{GaAs} (mm)	1.1	1.1	1.1	1.1	0.5	0.5
d_{GaSb} (μm)	0.95	0.94	0.98	0.68	1.98	1.87
d_{SL} (μm)	2.86	3.10	3.95	2.97	2.66	2.55

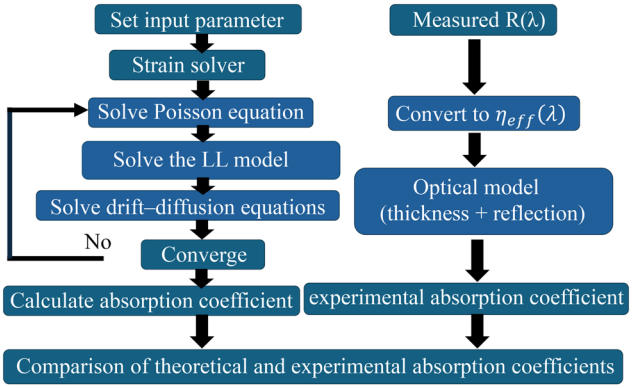

Fig. 2 Schematic illustration of the theoretical and experimental workflows used to extract and compare absorption coefficients. The left branch represents the simulation workflow of the coupled strain, Poisson, LL, drift-diffusion model, while the right branch shows the extraction procedure from measured responsivity.

the LL approach is adopted. Within this framework, strain effects on the electronic structure are described using deformation potential theory, as given in eqn (1),

$$H_{\varepsilon}^{\alpha\beta} = \sum_{i,j} D_{ij}^{\alpha\beta}\,\varepsilon_{ij} \tag{1}$$

Here, α and β denote band indices corresponding to different electronic bands, and H_{ε} represents the strain-induced perturbation to the Hamiltonian. The coefficients $D_{ij}^{\alpha\beta}$ are the deformation potential constants associated with the strain tensor ε_{ij}.

$$\Delta E_{\mathrm{c}} = a_{\mathrm{c}}(\varepsilon_{xx} + \varepsilon_{yy} + \varepsilon_{zz}), \tag{2}$$

$$\Delta E_{\upsilon,\mathrm{hh}} = a_{\upsilon}\left(\varepsilon_{xx} + \varepsilon_{yy} + \varepsilon_{zz}\right) + \frac{b}{2}\left(\varepsilon_{xx} + \varepsilon_{yy} - 2\varepsilon_{zz}\right), \tag{3}$$

$$\Delta E_{\upsilon,\mathrm{lh}} = a_{\upsilon}\left(\varepsilon_{xx} + \varepsilon_{yy} + \varepsilon_{zz}\right) - \frac{b}{2}\left(\varepsilon_{xx} + \varepsilon_{yy} - 2\varepsilon_{zz}\right), \tag{4}$$

where a_{c} and a_{υ} are the conduction band and valence band deformation potential under hydrostatic pressure, respectively. b is the shear deformation potential. E_{c} and E_{υ} are the conduction band and valence band potential before strain. $E'_{\upsilon,\mathrm{hh}}$ and $E'_{\upsilon,\mathrm{lh}}$ are the valence band potentials of heavy hole and light hole after strain, respectively, where the two bands are split.

The electrostatic potential ϕ is determined from the Poisson equation in eqn (5), which describes the potential distribution arising from the local carrier and ionized dopant densities

$$\nabla\cdot(\varepsilon_{\mathrm{r}}\nabla\phi) = q(n - p + N_{\mathrm{A}}^{-} - N_{\mathrm{D}}^{+}), \tag{5}$$

where n and p are the electron and hole densities, and N_{A}^{-} and N_{D}^{+} denote the ionized acceptor and donor densities, respectively. Here, ε_{r} is the dielectric permittivity of the material. Once the ϕ is obtained, E_{c} and E_{υ} are parallel to $-q\phi$. The band offset issue will be treated in the program.

To calculate the effective bandgap in SL, the $k{\cdot}p$ model or single band Schrödinger solver is used to solve the eigenvalue and eigen wavefunctions. In ref. 22, Filoche *et al.* propose the LL model, and they proved that instead of solving the eigenvalues of $H\psi = E\psi$, the LL model solves $Hu = 1$. And $1/u$ can be denoted as effective quantum potentials. Details of the LL model can be found in ref. 15–17, 23 and 24. Hence, we can obtain the effective quantum potential by solving

$$\left(-\frac{\hbar^2}{2}\nabla\left(\frac{1}{m_{\mathrm{e}}^{*}}\nabla\right) + (E_{\mathrm{c}} + \Delta E_{\mathrm{c}})\right)u_{\mathrm{e}} = 1, \tag{6}$$

$$\left(\frac{\hbar^2}{2}\nabla\left(\frac{1}{m_{\mathrm{hh}}^{*}}\nabla\right) - (E_{\upsilon} + \Delta E_{\upsilon,\mathrm{hh}})\right)u_{\mathrm{hh}} = 1, \tag{7}$$

$$\left(\frac{\hbar^2}{2}\nabla\left(\frac{1}{m_{\mathrm{lh}}^{*}}\nabla\right) - (E_{\upsilon} + \Delta E_{\upsilon,\mathrm{lh}})\right)u_{\mathrm{lh}} = 1, \tag{8}$$

where $\hbar$ is the reduced Planck constant, m_{e}^{*}, m_{hh}^{*}, and m_{lh}^{*} are the electron, heavy hole, and light hole effective masses, respectively.

After obtaining $1/u$, the electron and hole densities are calculated in the energy domain using the Fermi–Dirac distribution functions $f_{\mathrm{n}}(E, E_{\mathrm{fn}})$ and $f_{\mathrm{p}}(E, E_{\mathrm{fp}})$, together with the corresponding density of states $N_{\mathrm{c,dos}}(E)$ and $N_{\upsilon,\mathrm{dos}}(E)$, as expressed in eqn (9) and (10) The quantities E_{fn} and E_{fp} represent the quasi-Fermi levels for electrons and holes, respectively.

$$n = \int_{-\infty}^{\frac{1}{u_{\mathrm{e}}}} N_{\mathrm{c,dos}}(E)\cdot f_{\mathrm{e}}(E, E_{\mathrm{fn}})\mathrm{d}E \tag{9}$$

$$p = \int_{-\infty}^{\frac{1}{u_{\mathrm{hh}}}} N_{\upsilon,\mathrm{dos,hh}}(E)\cdot f_{\mathrm{p}}(E, E_{\mathrm{fp}})\mathrm{d}E + \int_{-\infty}^{\frac{1}{u_{\mathrm{lh}}}} N_{\upsilon,\mathrm{dos,lh}}(E)\cdot f_{\mathrm{p}}(E, E_{\mathrm{fp}})\mathrm{d}E \tag{10}$$

The quasi-Fermi levels E_{fn} and E_{fp} are obtained by solving the drift-diffusion equations in eqn (11) and (12), where the electron and hole current densities are driven by the gradients of the quasi-Fermi levels. These current densities are then incorporated into the continuity equation in eqn (13), which accounts for carrier transport under generation and recombination, where μ_{n} and μ_{p} are the electron and hole mobilities. G is the generation rate, and R is the total recombination rate.

$$J_{\mathrm{n}} = n\mu_{\mathrm{n}}\nabla E_{\mathrm{fn}} \tag{11}$$

$$J_{\mathrm{p}} = p\mu_{\mathrm{p}}\nabla E_{\mathrm{fp}} \tag{12}$$

$$\nabla\cdot J_{\mathrm{n,p}} = -q(R - G) \tag{13}$$

After convergence of the coupled equations, the band profile and LL-derived effective quantum potentials are obtained, based on which the optical absorption coefficients

$\alpha(\hbar\omega)$ are evaluated by considering transitions between the conduction and valence states. In ref. 25, the author further prove that by treating the effective bandgap $E_g^{\text{eff}}(r) = \frac{1}{u_e(r)} - \frac{1}{u_h(r)}$, we can further obtain the absorption coefficient:

$$\alpha\left(\hbar\omega, E_g^{\text{eff}}\right) = \frac{1}{d_{SL}}\frac{2}{3}\frac{e^2\hbar}{2m_0\varepsilon_0 c n_r}\int \frac{E_p}{\hbar\omega}\frac{\sqrt{2}m_r^{*3/2}}{\pi^2\hbar^3}\int \frac{1}{\sqrt{2\pi}\sigma}\exp\left(-\frac{(\hbar\omega - E)^2}{2\sigma^2}\right)\sqrt{E - E_g^{\text{eff}}(r)}\,dE\,dr \quad (14)$$

$\alpha(\hbar\omega)$ is the absorption coefficient obtained from the LL model. E_p is the material parameter related to the interband momentum matrix element. m_r^* is the reduced mass of the electron–hole system. ε_0 is the vacuum permittivity. m_0 is the free electron rest mass, and n_r is the real part of the refractive index of the material. c is the speed of light in vacuum. $\hbar\omega$ is the photon energy. Since the heavy hole band and light hole bands are split, the $\alpha_{\text{total}}(\hbar\omega)$ is further modified to

$$\alpha_{\text{total}}(\hbar\omega) = \alpha_{\text{c-hh}}\left(\hbar\omega, E_{\text{g,c-hh}}^{\text{eff}}\right) + \alpha_{\text{c-lh}}\left(\hbar\omega, E_{\text{g,c-lh}}^{\text{eff}}\right), \quad (15)$$

$$E_{\text{g,c-hh}}^{\text{eff}} = \left(\frac{1}{u_e} - \frac{1}{u_{hh}}\right), \quad (16)$$

$$E_{\text{g,c-lh}}^{\text{eff}} = \left(\frac{1}{u_e} - \frac{1}{u_{lh}}\right), \quad (17)$$

where $\alpha_{\text{c-hh}}$ is the absorption coefficient from heavy hole band to conduction band. $\alpha_{\text{c-lh}}$ is the absorption coefficient from light hole band to conduction band. The Gaussian broadening is also considered in absorption calculation, where the broadening σ is used. Since the experimentally measured quantity is the responsivity, the absorption coefficient cannot be obtained directly. Therefore, the procedure illustrated in the right panel of Fig. 2 is adopted to convert the measured responsivity into the absorption coefficient for comparison with the LL model.

Since the investigated devices are photoconductors, the measured responsivity inherently includes the contribution of photoconductive gain,[26] and can be expressed as

$$R(\lambda) = \frac{e\lambda}{hc}\eta(\lambda)\times g, \quad (18)$$

where $\eta(\lambda)$ is the quantum efficiency per incident photon absorbed and convert into electron–hole pair or we can call it as absorptance. g is the photoconductive gain, which converts the absorbed carrier into measured current density. Here, $R(\lambda)$ is the measured responsivity including photoconductive gain effects, h is Planck's constant, c is the speed of light in vacuum, and λ is the wavelength. Furthermore, $g = \frac{\tau}{t_t}$ is the photoconductive gain, where τ is free the carrier lifetime and t_t is the carrier transit time between ohmic contacts. The $\eta(\lambda)$ is related to the absorption coefficient, which can be written as

$$\eta(\lambda) = (1 - R_f)\left(1 - e^{-\alpha(\lambda)d_{SL}}\right)\times\frac{\left(1 + R_{b,\text{eff}}e^{-\alpha(\lambda)d_{SL}}\right)}{1 - R_f R_{b,\text{eff}}e^{-2\alpha(\lambda)d_{SL}}} \quad (19)$$

where d_{SL} represents the physical thickness of the SL absorber. In the photon energy range below 0.7 eV, GaAs and GaSb are assumed to be non-absorbing because the energy is below bandgap.[27–29] And $\eta(\lambda) \times g$ represents the combined effect of carrier generation efficiency and photoconductive gain contributing to the photocurrent. R_f is the front-surface reflectance, and $R_{b,\text{eff}}$ is defined as the overall effective back-side reflectance seen by light transmitted through the superlattice toward the substrate side.

$$R_{b,\text{eff}} = R_{\text{GaSb/GaAs}} + \frac{\left(1 - R_{\text{GaSb/GaAs}}\right)^2 R_{\text{back}}}{1 - R_{\text{GaSb/GaAs}}R_{\text{back}}} \quad (20)$$

In the present model, $R_{b,\text{eff}}$ accounts for the wavelength-dependent refractive indices at the GaSb/GaAs interface,[30–32] as well as the non-ideal optical interface between the GaAs substrate and the silver paste attached to the thermoelectric cooler. The back-side reflectance, denoted as R_{back}, is defined as the reflectance associated with this non-ideal optical interface. Due to surface roughness, particle aggregation, and the non-continuous morphology of the silver paste,[33] R_{back} is treated as an effective parameter and is reasonably assumed to be approximately 0.85. The correctness of eqn (19) and (20) was verified using RCWA.[34,35] In practice, however, the Fabry–Perot resonance predicted by RCWA was less pronounced, primarily due to surface roughness and non-ideal optical interfaces. Consequently, the measured absorptance spectrum more closely follows the averaged response, which is in better agreement with eqn (19). Therefore, an effective reflectance parameter $R_{b,\text{eff}}$ was directly adopted in the fitting procedure.

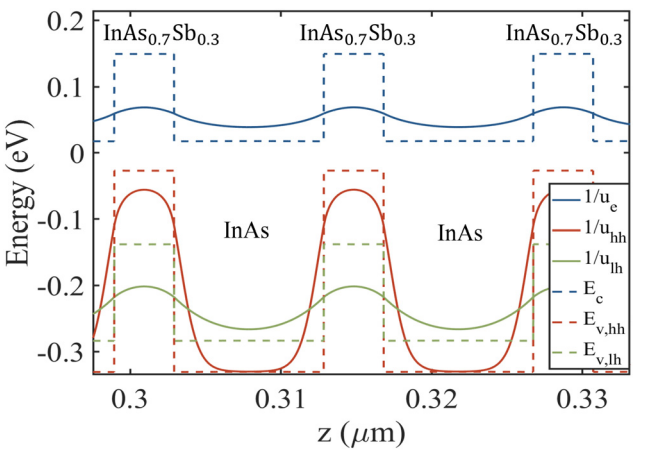

Fig. 3 The quantum potentials $1/u_e$, $1/u_{hh}$, and $1/u_{lh}$ represent the effective quantum potentials for electrons, heavy holes, and light holes, respectively.

A. Simulation results of the LL model

As an example, the LWIR L-8.7 structure is considered to illustrate the band profile obtained using the LL approach. As shown in Fig. 3, the strain-modified conduction band edge E_c' and valence band edges $E_{v,hh}'$ and $E_{v,lh}'$ are presented together with the corresponding effective quantum potentials $\frac{1}{u_e}$, $\frac{1}{u_{v,hh}}$, and $\frac{1}{u_{v,lh}}$ for electrons, heavy holes, and light holes, respectively.

The results exhibit the characteristic type-II band alignment of the InAs/InAs1$_{-y}$Sb$_y$ SL, in which electrons are primarily confined within the InAs layers, while holes are mainly localized in the InAsSb layers, leading to a spatial separation of carriers. This behavior is clearly reflected in the landscape potentials: the electron effective potential $\frac{1}{u_e}$, shows relatively smooth spatial variation, indicating weaker confinement, whereas $\frac{1}{u_{v,hh}}$ and $\frac{1}{u_{v,lh}}$ exhibit pronounced localization within the InAs1$_{-y}$Sb$_y$ regions, corresponding to stronger hole confinement.

The effective quantum potentials obtained by the LL model, providing direct insight into carrier localization and effective band-edge profiles without explicitly solving the Schrödinger equation. The SL period directly controls the effective bandgap through quantum confinement. In addition, the alloy composition of InAs1$_{-y}$Sb$_y$ influences both the band alignment and the strain distribution, thereby further modifying the band structure.[36]

B. Experimental responsivity

In the following analysis, we consider experimentally measured responsivity spectra from LWIR and MWIR photodetectors. The datasets are grouped by spectral regime to facilitate direct comparisons within each regime. The spectral responsivity of the fabricated devices is measured and summarized in Fig. 4(a) for the LWIR datasets and Fig. 4(b) for the MWIR datasets. Within each spectral regime, multiple experimental datasets are presented concurrently to enable systematic comparison of cutoff behavior. These experimentally measured spectra constitute the experimental basis for the subsequent extraction of absorption coefficients and quantitative comparison with theoretical models.

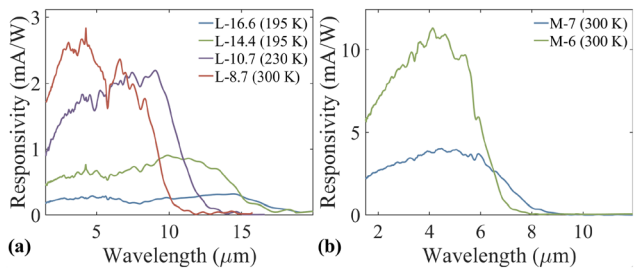

Fig. 4 Measured spectral responsivity of SL photodetectors. (a) LWIR devices and (b) MWIR devices, showing multiple experimental datasets within each spectral regime.

Table 2 Material parameters of the binary endpoints used in the calculations[41–43]

Parameter	InAs	InSb
a (Å)	6.058	6.479
a_c (eV)	−5.08	−6.94
a_v (eV)	−1.0	−0.36
b (eV)	−1.8	−2.0
χ (eV)	4.9	4.59
m_e (m_0)	0.027	0.014
$m_{hh,z}$ (m_0)	0.3333	0.2632
$m_{hh,\|\|}$ (m_0)	0.0351	0.0199
$m_{lh,z}$ (m_0)	0.027	0.0152
$m_{lh,\|\|}$ (m_0)	0.087	0.0518
E_p (eV)	21.5	23.3
n	3.4	4.0

Bandgap bowing term b_{E_g} = 0.67 eV
Electron affinity bowing term b_χ = −0.2262 eV

C. Comparison between experimentally extracted absorption coefficient and the LL model

To establish a consistent and unambiguous basis for comparison, the experimental and theoretical absorption coefficients are obtained through two distinct and complementary procedures. The theoretical absorption coefficient is constructed within the LL framework using eqn (14), which directly yields the optical absorption as a function of photon energy based on the effective bandgap landscape. All material parameters required for the LL-based absorption model, including the Kane energy and carrier effective masses, are summarized in Tables 3 and 1 (see Appendix). On the experimental side, the measured spectral responsivity $R(\lambda)$ is converted into the experimental absorption coefficient α_{ex} by numerically solving eqn (18) and (19). with the corresponding parameters summarized in Table 3 (see Appendix). By combining the material parameters (Tables 2 and 3) with the geometric and structural properties of the InAs/InAsSb T2SL samples (Table 1), the LL-predicted absorption coefficients can be directly compared with experimental results. The parameters used in the absorption coefficient calculations are listed in Tables 2 and 3. Most

Table 3 Sample-specific parameters, including Sb composition, temperature, Gaussian broadening, and band edge shifts

Sample	y_{Sb}	T (K)	σ (eV)	ΔE_c (eV)	$\Delta E_{v,hh}$ (eV)	$\Delta E_{v,lh}$ (eV)
L-16.6	0.42	195	0.18 k_BT	0.1041	0.0728	−0.1024
L-14.4	0.44	195	0.18 k_BT	0.1114	0.0775	−0.1084
L-10.7	0.38	230	0.4 k_BT	0.09	0.0633	−0.0904
L-8.7	0.30	300	0.45 k_BT	0.0629	0.0449	−0.066
M-7	0.35	300	0.45 k_BT	0.0796	0.0563	−0.0813
M-6	0.335	300	0.45 k_BT	0.0745	0.0529	−0.0767

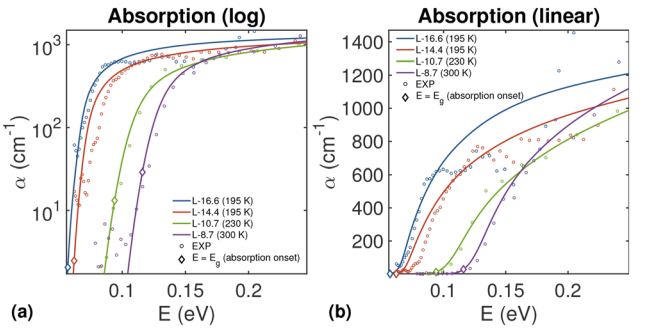

Fig. 5 Comparison of LWIR absorption coefficients between LL calculations and experiments shown on (a) logarithmic and (b) linear scales.

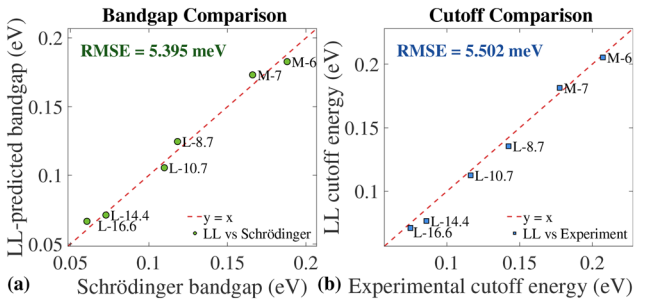

Fig. 7 Parity plots comparing the LL predictions with reference results: (a) bandgap *versus* Schrödinger calculations and (b) cutoff energy *versus* experiment, where the cutoff is defined at the half-maximum responsivity.

values are obtained by linear interpolation between InAs and InSb, while bowing terms are applied to electron affinity and bandgap to account for their nonlinear composition dependence. The g is required. At shorter wavelength, the absorption coefficient is larger, where the absorptance approaching the maximum can be expected.

The results are shown in in Fig. 9. For longer wavelengths, where absorption is incomplete, the average g obtained from the shorter-wavelength regime is used to estimate α_{ex}. This approximation may influence the absolute magnitude of α_{ex}, but it does not affect the cutoff position of the absorption band edge.

Fig. 5 and 6 illustrate the direct comparison between the experimentally extracted absorption coefficients and the theoretical spectra calculated using LL framework for the LWIR and MWIR samples (see Appendix for details of the methodology and validation). In both spectral ranges, the LL calculations exhibit band-edge (absorption-onset) features at energy positions consistent with the experimental results and capture the corresponding spectral evolution, supporting the use of the LL framework to describe the absorption behaviour near the band edge. The diamond markers denote the minimum bandgap energy E_g. The finite absorption observed for $E < E_g$ originates from Gaussian broadening of the band-edge transitions. To further validate the LL model, the LL-predicted cutoff energies were compared with the experimentally determined values. Fig. 7 illustrates the parity plot for the six representative samples, providing a visual assessment of the model's predictive accuracy.

As shown in Fig. 7(a), the LL-predicted bandgaps exhibit excellent agreement with the Schrödinger-based results, with a root-mean-square error (RMSE) of 5.395 meV. This confirms that the LL framework can accurately capture the minimum optically active transition energy across both LWIR and MWIR samples. The cutoff energy comparison in Fig. 7(b), defined using the half-maximum responsivity criterion, also demonstrates good agreement, with an RMSE of 5.502 meV. For consistency, the cutoff energy of the LL results is extracted by first converting the LL-derived absorption coefficient into the corresponding optical response and subsequently identifying the energy at half of the maximum responsivity. A slightly larger deviation is observed in the MWIR region, which can be attributed to the sharper spectral drop near the cutoff, making the extracted cutoff energy more sensitive to variations in spectral shape. Overall, these results demonstrate the robustness of the LL framework in accurately predicting both the effective bandgap and the device-level optical response.

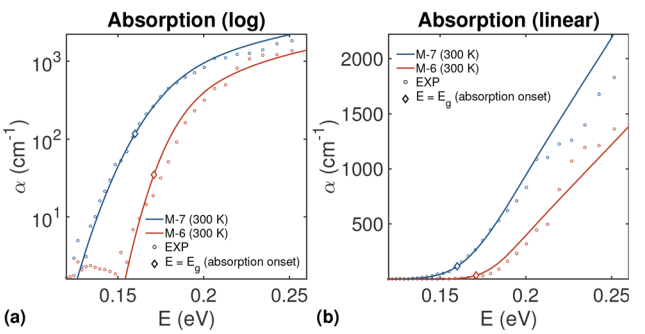

Fig. 6 Comparison of MWIR absorption coefficients between LL calculations and experiments shown on (a) logarithmic and (b) linear scales.

IV. Conclusion

In this work, the LL framework was applied to analyze optical absorption in MWIR and LWIR InAs/InAsSb T2SL absorbers. Within the effective-mass approximation, the LL formalism provided physically transparent effective band landscapes that capture carrier localization and band-edge formation without solving the full Schrödinger equation. Direct comparison with experimentally extracted absorption coefficients confirmed that the LL model reproduces both the spectral evolution and the absorption onset across a broad IR range. Quantitative validation showed excellent agreement: the LL-predicted bandgaps matched Schrödinger calculations with an RMSE of 5.395 meV, while cutoff energies agreed with experiment within 5.502 meV. These results demonstrate that the LL framework provides a computationally efficient and physically consistent alternative to eigenstate-based solvers, enabling robust modeling of

disordered superlattice absorbers and serving as a practical tool for the design and optimization of large-scale infrared photodetectors.

V. Appendix

A. Material and optical parameters

The material and optical parameters used in this work are summarized in Tables 2 and 3. The refractive index, front-surface reflectance, Kane energy E_p, lattice constant, and deformation potential parameters of $InAs_{1-y}Sb_y$ are treated as composition-dependent quantities obtained through linear interpolation between the corresponding binary compounds.

The effective masses are evaluated using inverse linear interpolation between the binary endpoints and are applied to all band components. In zinc blende structures, the in-plane directions are isotropic, and thus the in-plane effective masses are taken as $m_{hh,\|} = m_{hh,x} = m_{hh,y}$ and $m_{lh,\|} = m_{lh,x} = m_{lh,y}$.

For the InAsSb alloy, key band parameters, including the electron affinity and the bandgap, are composition dependent and exhibit non-linear behavior due to alloy effects.[37] In this work, these quantities are described using bowing-type interpolation expressions:

$$\chi(y) = \chi_{InSb}\cdot y + \chi_{InAs}(1-y) - b_\chi y(1-y) \quad (21)$$

$$E_g(y) = E_{g,InSb}\cdot y + E_{g,InAs}(1-y) - b_{E_g} y(1-y) \quad (22)$$

where $E_g(y)$ and $\chi(y)$ denote the bandgap and electron affinity of $InAs1_{-y}Sb_y$, respectively, $E_{g,InAs}$ and $E_{g,InSb}$ are the bandgaps of the binary compounds, χ_{InAs} and $_{InSb}$ are the corresponding electron affinities, and b_{E_g} and b_χ are the associated bowing parameters.

In addition, Gaussian broadening is used to account for thermal effects and disorder-induced band-edge smearing,[38,39] where the broadening width σ is taken to be proportional to temperature.[40]

E'_c, $E'_{v,hh}$, and $E'_{v,lh}$ in the above table represent the strain-induced shifts of the conduction band and valence band edges at the Γ point, where the strain is defined with respect to the GaSb buffer layer.

The experimental $\eta(\lambda) \times g$ spectra shown in Fig. 8 were obtained from the measured responsivity using eqn (18),

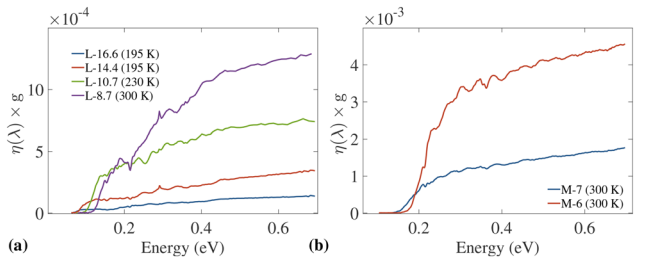

Fig. 8 $\eta(\lambda) \times g$ as a function of photon energy for (a) LWIR and (b) MWIR devices.

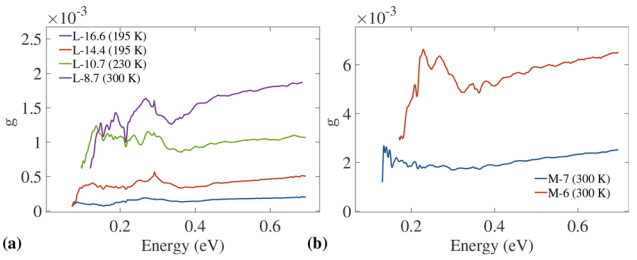

Fig. 9 Extracted g of the MWIR and LWIR samples by assuming the absorption coefficient calculated by the LL model is accurate.

followed by wavelength-to-energy conversion. To extract the absorption coefficient, however, the gain must first be determined, and then η and α can be obtained using eqn (19). A condition where the gain is independent of the absorption coefficient arises when the absorption is sufficiently strong to reach the maximum η. This maximum occurs when all incident light is absorbed before reflection from the back reflector. For example, in the M-7 case, $\eta(\lambda) \times g$ begins to saturate for $\hbar\omega > 0.3$ eV. The maximum absorption can be expressed as

$$\eta_{max} = (1 - R_f), \quad (23)$$

where most incident light is absorbed. Hence, the gain can be estimated near $\hbar\omega = 0.3$ eV, and this value may be assumed to apply for $\hbar\omega < 0.3$ eV to obtain the absorption coefficient in that regime.

To further verify this, Fig. 9 shows the calculated gain obtained by using the absorption coefficient calculated by the LL model.

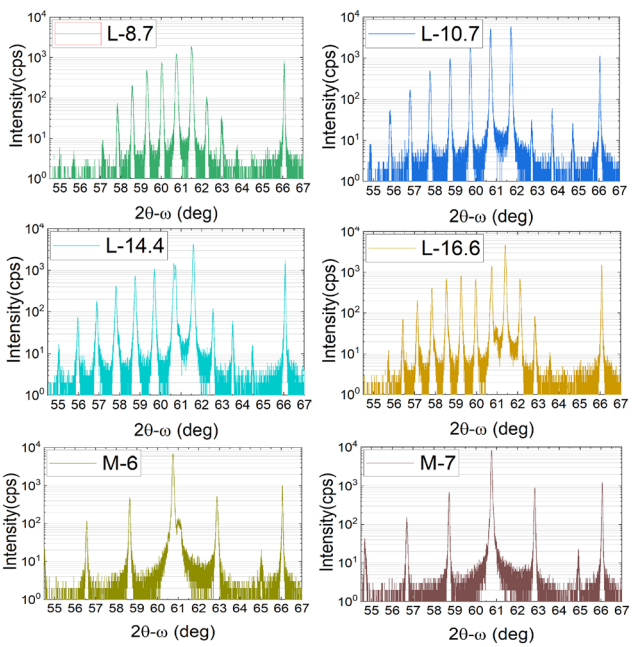

Fig. 10 High-resolution X-ray diffraction (HRXRD) 2θ–ω scans of the investigated LWIR and MWIR InAs/InAsSb superlattice samples.

As shown in Fig. 9, above the absorption saturation region, the gain is smooth and slightly increases as $\hbar\omega$ increases. This increase may be attributed to improved carrier extraction, since absorbed carriers are closer to the surface and the contact. Therefore, a representative value of g is obtained by averaging g over a selected energy window near the onset of the saturation region. This averaged value is then used as the effective gain of the device to extract the absorption coefficient below the saturation region. The oscillations observed below saturation may be due to a weak Fabry–Perot mode. Using this obtained gain, g, the experimental absorption coefficient is determined by numerically inverting eqn (19). The resulting absorption spectra are presented in Fig. 5 and 6.

Since the photoconductive gain is defined as $g = \frac{\tau}{t_t}$, different combinations of $\eta(\lambda)$ and g can produce similar responsivity spectra. Thus, measured responsivity mainly reflects the combined quantity $\eta(\lambda) \times g$. Even if the carrier continuity equations are solved self-consistently, transport and recombination parameters must still be assumed or fitted. Consequently, $\eta(\lambda)$ and photoconductive gain cannot be uniquely separated from responsivity or $\eta(\lambda) \times g$ spectra alone, except in the regime above the saturation region where separation becomes possible.

B. HRXRD characterization

All investigated samples exhibit clear superlattice satellite peaks in the HRXRD 2θ–ω scans, indicating good periodicity and interface quality of the InAs/InAsSb superlattices. The well-defined higher-order diffraction peaks further suggest relatively uniform layer thicknesses and good structural coherence throughout the absorber region.

Conflicts of interest

There are no conflicts to declare.

Data availability

All input files used in the simulations are in the supplementary material or are available from the corresponding author upon reasonable request. The simulation software employed in this study can be downloaded from the corresponding author's group website at https://yrwu-wk.ee.ntu.edu.tw/index.php/download-ntu-itri-ddcc/.

Supplementary information (SI): the input setting file for 6 cases to run in the DDCC simulation program is provided in the supplemental materials. See DOI: https://doi.org/10.1039/d6lf00119j.

Acknowledgements

This work is supported by the National Science and Technology Council, Taiwan, (NSTC) under grant 112-2923-E-002-008-MY3, 114-2622-8-002-016, 115-2119-M-002-003, and 112-2221-E-002-215-MY3. Prof. Yuh-Renn Wu is also supported by the Leap fellowship of the Foundation for the Advancement of Outstanding Scholarship. This work was also supported by the Polish National Centre for Research and Development grant POLTAJ10/2022/37/LWIRPSBDA/2023.

References

1 J. Jiang, K. Liu, L. Zhou, Y. Zhao, R. Li, T. Li, D. Wu, G. Wang, D. Jiang, H. Hao, Y. Xu and Z. Niu, InAs/InAsSb type-II superlattice mid-wavelength infrared photodetectors with high antimony component absorber quantum efficiency enhancement, *J. Cryst. Growth*, 2025, **666**, 128228.
2 S. A. Pour, E. K. Huang, G. Chen, A. Haddadi, B.-M. Nguyen and M. Razeghi, High operating temperature midwave infrared photodiodes and focal plane arrays based on type-II InAs/GaSb superlattices, *Appl. Phys. Lett.*, 2011, **98**, 143501.
3 A. Rogalski, M. Kopytko, W. Hu and P. Martyniuk, Infrared HOT photodetectors: status and outlook, *Sensors*, 2023, **23**, 7564.
4 A. Rogalski, M. Kopytko, F. Dai, R. Jiang, F. Wang, W. Hu and P. Martyniuk, Infrared HOT material systems vs. Law 19 paradigm, *Measurement*, 2024, **230**, 114495.
5 X. Xue, M. Chen, Y. Luo, T. Qin, X. Tang and Q. Hao, High operating-temperature mid-infrared photodetectors via quantum dot gradient homojunction, *Light: Sci. Appl.*, 2023, **12**, 2.
6 J. Jiang, G. Wang, D. Wu, Y. Xu, F. Chang, W. Zhou, N. Li, D. Jiang, H. Hao and S. Cui, *et al.*, High-performance infrared pho to detectors based on InAs/InAsSb/AlAsSb superlattice for 3.5 μm cutoff wavelength spectra, *Opt. Express*, 2022, **30**, 38208–38215.
7 B. C. Connelly, G. D. Metcalfe, H. Shen and M. Wraback, Direct minority carrier lifetime measurements and recombination mechanisms in long-wave infrared type II superlattices using time-resolved photoluminescence, *Appl. Phys. Lett.*, 2010, **97**, 251117.
8 A. Rogalski, α/G figure of merit for infrared photodetector materials, *J. Appl. Phys.*, 2025, **137**, 170701.
9 E. Steenbergen, B. Connelly, G. Metcalfe, H. Shen, M. Wraback, D. Lubyshev, Y. Qiu, J. Fastenau, A. Liu and S. Elhamri, *et al.*, Significantly improved minority carrier lifetime observed in a long-wavelength infrared III-V type-II superlattice comprised of InAs/InAsSb, *Appl. Phys. Lett.*, 2011, **99**, 251110.
10 G. Cao, *Nanostructures & nanomaterials: synthesis, properties & applications*, Imperial College Press, 2004.
11 B. Liu, L. Zhu, Y. Liu, L. Lu, R. Gong, H. An, D. Zhang, X. Zheng, Y. Feng and M. Dong, Temperature dependent growth of InAs/InAsSb superlattices by molecular beam epitaxy for HOT mid-wavelength infrared detectors, *Mater. Sci. Semicond. Process.*, 2023, **163**, 107590.
12 Y. Zhang, Y. Shan, F. Chang, Y. Liang, X. Zhang, G. Wang, D. Wu, D. Jiang, H. Hao and Y. Xu, *et al.*, Improvement of mid wavelength InAs/InAsSb nBn infrared detectors performance through interface control, *Infrared Phys. Technol.*, 2024, **143**, 105619.

13 M. Kopytko, G. Kołodziej, P. Baranowski, K. Murawski, Ł. Kubiszyn, K. Michalczewski, B. Seredyński, K. Szlachetko, J. Jureńczyk and W. Gawron, LWIR InAs/InAsSb Superlattice Detector for Cooled FPA, in *Proceedings*, MDPI, 2025, vol. 129, p. 28.
14 D. N. Arnold, G. David, D. Jerison, S. Mayboroda and M. Filoche, Effective confining potential of quantum states in disordered media, *Phys. Rev. Lett.*, 2016, **116**, 056602.
15 M. Filoche, M. Piccardo, Y.-R. Wu, C.-K. Li, C. Weisbuch and S. Mayboroda, Localization landscape theory of disorder in semiconductors. I. Theory and modeling, *Phys. Rev. B*, 2017, **95**, 144204.
16 C.-K. Li, M. Piccardo, L.-S. Lu, S. Mayboroda, L. Martinelli, J. Peretti, J. S. Speck, C. Weisbuch, M. Filoche and Y.-R. Wu, Localization landscape theory of disorder in semiconduc tors. III. Application to carrier transport and recombination in light emitting diodes, *Phys. Rev. B*, 2017, **95**, 144206.
17 M. Piccardo, C.-K. Li, Y.-R. Wu, J. S. Speck, B. Bonef, R. M. Farrell, M. Filoche, L. Martinelli, J. Peretti and C. Weisbuch, Localization landscape theory of disorder in semiconductors. II. Urbach tails of disordered quantum well layers, *Phys. Rev. B*, 2017, **95**, 144205.
18 D. Z. Ting, S. B. Rafol, A. Khoshakhlagh, A. Soibel, S. A. Keo, A. M. Fisher, B. J. Pepper, C. J. Hill and S. D. Gunapala, InAs/InAsSb Type-II Strained-Layer Superlattice Infrared Pho to detectors, *Micromachines*, 2020, **11**, 958.
19 J. A. Keen, D. Lane, M. Kesaria, A. R. J. Marshall and A. Krier, InAs/InAsSb type-II strained-layer superlattices for mid-infrared LEDs, *J. Phys. D: Appl. Phys.*, 2018, **51**, 075103.
20 L. K. Casias, C. P. Morath, E. H. Steenbergen, G. A. Umana Membreno, P. T. Webster, J. V. Logan, J. K. Kim, G. Balakrishnan, L. Faraone and S. Krishna, Vertical carrier transport in strain-balanced InAs/InAsSb type-II superlattice material, *Appl. Phys. Lett.*, 2020, **116**, 182109.
21 D. Kwan, M. Kesaria, J. Jiménez, V. Srivastava, M. Delmas, B. Liang, F. Morales and D. Huffaker, Monolithic integration of a 10 μm cut-off wavelength inas/gasb type-ii superlattice diode on gaas platform, *Sci. Rep.*, 2022, **12**, 11616.
22 M. Filoche and S. Mayboroda, Universal mechanism for Ander son and weak localization, *Proc. Natl. Acad. Sci. U. S. A.*, 2012, **109**, 14761–14766.
23 T.-Y. Tsai, K. S. Qwah, J.-P. Banon, M. Filoche, C. Weisbuch, Y.-R. Wu and J. S. Speck, Carrier localization in III-nitride versus conventional III-V semiconductors: A study on the effects of alloy disorder using landscape theory and the Schrödinger equation, *Phys. Rev. Appl.*, 2023, **20**, 044069.
24 H.-C. Huang, S.-M. Chen, C. Weisbuch, J. S. Speck and Y. R. Wu, The influence of V-defects, leakage, and random alloy fluctuations on the carrier transport in red InGaN MQW LEDs, *Appl. Phys. Rev.*, 2025, **12**, 031402.
25 J.-P. Banon, P. Pelletier, C. Weisbuch, S. Mayboroda and M. Filoche, Wigner-Weyl description of light absorption in disordered semiconductor alloys using the localization landscape theory, *Phys. Rev. B*, 2022, **105**, 125422.
26 G. Ariyawansa, M. Grupen, J. M. Duran, J. E. Scheihing, T. R. Nelson and M. T. Eismann, Design and modeling of InAs/GaSb type II superlattice based dual-band infrared detectors, *J. Appl. Phys.*, 2012, **111**, 073107.
27 M. Wasiak, M. Motyka, T. Smołka, J. Ratajczak and A. Jasik, Absorption and dispersion in undoped epitaxial GaSb layer, *Mater. Res. Express*, 2018, **5**, 025907.
28 C. Ghezzi, R. Magnanini, A. Parisini, B. Rotelli, L. Tarricone, A. Bosacchi and S. Franchi, Optical absorption near the fundamental absorption edge in GaSb, *Phys. Rev. B: Condens. Matter Mater. Phys.*, 1995, **52**, 1463.
29 M. Sturge, Optical absorption of gallium arsenide between 0.6 and 2.75 eV, *Phys. Rev.*, 1962, **127**, 768.
30 S. Adachi, Optical dispersion relations for GaP, GaAs, GaSb, InP, InAs, InSb, $Al_xGa_{1-x}As$, and $In_{1-x}Ga_xAs_yP_{1-y}$, *J. Appl. Phys.*, 1989, **66**, 6030–6040.
31 A. D. Rakić and M. L. Majewski, Modeling the optical dielectric function of GaAs and AlAs: Extension of Adachi's model, *J. Appl. Phys.*, 1996, **80**, 5909–5914.
32 D. F. Edwards and R. H. White, Gallium Antimonide (GaSb), in *Handbook of Optical Constants of Solids*, ed. E. D. Palik, Academic Press, 1997, pp. 597–606.
33 M. Dehghani and C. David, Light Scattering from Rough Silver Surfaces: Modeling of Absorption Loss Measurements, *Nanomaterials*, 2021, **11**, 113.
34 C.-H. Hsieh, J.-Y. Huang and Y.-R. Wu, Analysis of two terminal perovskite/silicon tandem solar cells with differing texture structure, perovskite carrier lifetime, and tunneling junction quality, *J. Appl. Phys.*, 2024, **135**, 115002.
35 H.-Y. Wang, H. Lee, P. Martyniuk and Y.-R. Wu, Di electric resonator antenna-coupled T2SL cascades for LWIR enhancement, *Jpn. J. Appl. Phys.*, 2026, DOI: 10.35848/1347-4065/ae6d61, in press.
36 T. Manyk, K. Michalczewski, K. Murawski, P. Martyniuk and J. Rutkowski, InAs/InAsSb strain-balanced superlattices for longwave infrared detectors, *Sensors*, 2019, **19**, 1907.
37 T. Manyk, K. Murawski, K. Michalczewski, K. Grodecki, J. Rutkowski and P. Martyniuk, Method of electron affinity evaluation for the type-2 $InAs/InAs_{1-x}Sb_x$ superlattice, *J. Mater. Sci.*, 2020, **55**, 5135–5144.
38 A. Canul, I. Lukman and L. Bergman, The Gaussian nature of the band-edge of ZnO microcrystalline thin films, *AIP Adv.*, 2022, **12**, 125201.
39 R. A. Redkin, N. I. Onishchenko, A. V. Kosobutsky, V. N. Brudnyi, X. Su and S. Y. Sarkisov, Temperature-Dependent Optical Absorption and DLTS Study of As-Grown and Electron Irradiated GaSe Crystals, *Crystals*, 2025, **15**, 372.
40 C. Grein and S. John, Temperature dependence of the Urbach optical absorption edge: A theory of multiple phonon absorption and emission sidebands, *Phys. Rev. B: Condens. Matter Mater. Phys.*, 1989, **39**, 1140.
41 S. Adachi, *Properties of semiconductor alloys: group-IV, III-V and II-VI semiconductors*, John Wiley & Sons, 2009.

42 P. Paskov, Refractive indices of InSb, InAs, GaSb, $InAs_xSb_{1-x}$, and $In_{1-x}Ga_xSb$: effects of free carriers, *J. Appl. Phys.*, 1997, **81**, 1890–1898.

43 I. Vurgaftman, J. R. Meyer and L. R. Ram-Mohan, Band parameters for III–V compound semiconductors and their alloys, *J. Appl. Phys.*, 2001, **89**, 5815–5875.